https://doi.org/10.32604/zkg.2026.075872

ARTICLE

Multi-method study on the effect of biochar on the properties of alkali-activated slag

Xu Yang[1,2,#], Feng Sun[3,#], Ki-Bong Park[2] and Xiao-Yong Wang[2,3,*]
[1]National Engineering Research Center for Marine Aquaculture, Zhejiang Ocean University, Zhoushan, China
[2]Department of Architectural Engineering, Kangwon National University, Chuncheon-si, Republic of Korea
[3]Department of Integrated Energy and Infra System, Kangwon National University, Chuncheon-si, Republic of Korea
*Corresponding Author: Xiao-Yong Wang. Email: wxbrave@kangwon.ac.kr
#These authors contributed equally to this work

Received: 10 November 2025; Accepted: 16 January 2026

ABSTRACT: Alkali-activated slag (AAS) is regarded as a promising low-carbon alternative to Portland cement; however, the increasing scarcity of slag and the need for further sustainability improvements motivate the exploration of renewable and carbon-based additives. Biochar, as a porous and carbon-rich material derived from biomass waste, has shown potential in cementitious systems, yet its role and mechanism in AAS remain insufficiently understood. To address this gap, a systematic experimental study was conducted to investigate the effects of biochar on the reaction kinetics, microstructure, and engineering properties of AAS. Biochar was used to partially replace slag at 1, 2, and 5 wt%. Isothermal calorimetry, XRD, FTIR, SEM, and TG analyses were employed to characterize reaction behavior and products, while workability, compressive strength, ultrasonic pulse velocity (UPV), electrical resistivity, and chloride diffusion tests were performed to evaluate macroscopic performance. The results showed that biochar increased the 7-day cumulative reaction heat and promoted late-age CASH formation, while not altering the main reaction products, indicating a predominantly physical role. The porous structure of biochar provided internal space for alkali activation but also introduced air bubbles during mixing, leading to reduced absolute compressive strength and UPV. Despite this strength reduction, moderate biochar additions (1–2 wt%) had limited adverse effects on durability-related properties and showed improved relative strength development at later ages. Overall, this study clarifies the mechanism by which biochar influences AAS systems and demonstrates the feasibility of partially replacing slag with biochar, providing guidance for the development of more sustainable alkali-activated materials.

KEYWORDS: Biochar, alkaline activated slag, reaction kinetics, properties, mechanism

MATERIALS

1 Introduction

As an alternative to Portland cement, alkali-activated materials (AAMs) have been extensively used because of their low-carbon footprint, outstanding mechanical properties, and durability [1]. Slag is a by-product of the metal smelting process and has been widely used in research as an alkali-activated precursor material. Compared to traditional cementitious materials, hardened alkali-activated slag (AAS) exhibits superior mechanical properties, durability, and high-temperature resistance [2]. The application of slag as a new resource for waste recycling in AAM is desirable. However, with the shortage and restricted development of mineral resources worldwide, slag, as a by-product of the industry, is becoming scarce.

As a green material, biochar has a wide range of raw materials, such as rice husk, peanut shell, and food waste biochar, which can facilitate the recycling of agricultural by-products and living waste. Biochar prepared under anaerobic or anoxic conditions is an effective means of achieving resource sustainability for agricultural by-products and living waste, compared to direct incineration or rot, which produces greenhouse gases or methane. The feasibility of applying green biochar to cementitious materials has been widely reported. Praneeth et al. investigated the compressive strength and CO_2 absorption capacity of biochar cement–fly ash composites; the results showed that the mechanical properties and CO_2 absorption capacity of the composites increased as the biochar substitution increased [3]. Biochar-modified cementitious materials not only improved the mechanical properties of the composites and achieved the effect of carbon sequestration, but also improved the acoustic and thermal properties. Cuthbertson et al. reported that the addition of biochar improved the sound absorption coefficient of concrete in the range of 200–2000 Hz and reduced the associated thermal conductivity [4]. Akinyemi and Adesina reviewed the application of biochar in cementitious materials and summarized the effects of different biochar raw materials, production processes, and dosages on

the performance of cementitious materials, indicating the feasibility and reasonableness of biochar as a sustainable admixture for cementitious materials [5].

Although the research on biochar in cement-based concrete materials has been relatively extensive, studies on biochar in alkali-activated materials remain limited. For instance, the effects of biochar on the micro- and macro-properties of alkali-activated materials, the mechanisms behind these effects, and the interconnections between microstructural and macroscopic behaviors still require further clarification. To fill these gaps, this study analyzed alkali-activated slag (AAS)–biochar binary mixtures using a series of comprehensive experimental techniques, including isothermal calorimetry, Fourier transform infrared spectroscopy (FTIR), X-ray diffraction (XRD), thermogravimetric analysis (TGA), scanning electron microscopy (SEM), optical microscopy, flowability, compressive strength, ultrasonic pulse velocity (UPV), electrical resistivity, and chloride diffusion tests.

Biochar-modified alkali-activated slag is intended for low-carbon applications prioritizing sustainability and durability. The performance tests were conducted to verify the feasibility and long-term applicability of biochar incorporation in AAS. In this study, sodium hydroxide and sodium silicate composite alkali activators were used, and different levels of biochar substitution (1, 2, and 5 wt%) were used to replace the alkali-activated precursor material slag. The effect of green material biochar on the mechanism of the AAS system was investigated by comparing the reaction heat and kinetic analysis, reaction products, workability, mechanical properties, and durability of plain AAS and AAS biochar. The feasibility of partial replacement of slag in alkali-activated systems by biochar is discussed. This study provides a new idea for applying biochar in construction engineering and provides the basis for future research on the potential application of biochar to AAMs.

2 Materials and methods

2.1 Materials

In this study, blast furnace slag was used as the geopolymer precursor in the alkali-activated system, while biochar served as a partial replacement for slag. The slag and biochar were supplied by Asia Cement Co., Ltd. and Yougi Company, respectively. The particle size distributions of slag and laboratory-ground biochar were measured using a Mastersizer 3000 laser diffraction analyzer, as shown in Figure 1. The slag particles ranged from 0.523 to 66.9 µm with a DV50 of 12.3 µm, whereas the biochar particles ranged from 0.523 to 127 µm with a DV50 of 18.7 µm. The chemical compositions of slag and biochar were determined by X-ray fluorescence (ZSX Primus II), and the results are summarized in Table 1. The micromorphologies observed by scanning electron microscopy (Hitachi S-4800) are presented in Figure 2, showing angular and irregular particles

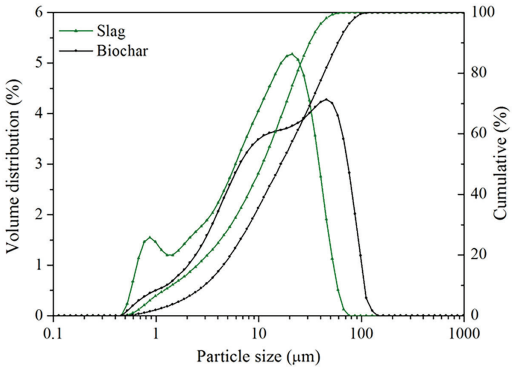

1 Particle size distribution of cement and biochar

Table 1 Chemical composition of cement and biochar

Chemical composition (%)	Slag	Biochar
CaO	39.60	0.20
SiO_2	33.43	18.97
Al_2O_3	16.21	0.04
SO_3	2.65	0.13
MgO	7.10	0.10
P_2O_5	–	0.16
Fe_2O_3	0.65	0.05
K_2O	0.60	1.19
TiO_2	0.44	–
ZrO_2	0.05	–
CO_2	–	78.97
MnO	0.20	0.06
Cl	–	0.09
Na_2O	0.30	0.04
LOI	–1.23	

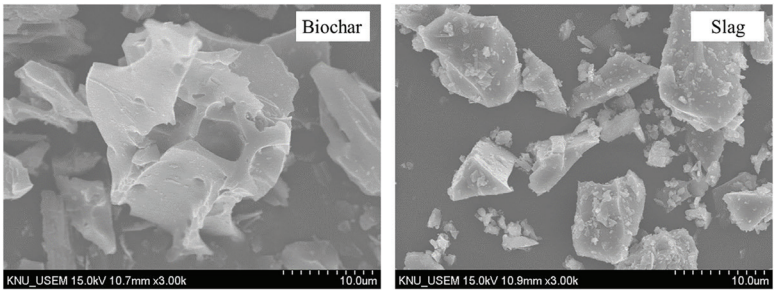

2 Slag and biochar SEM images

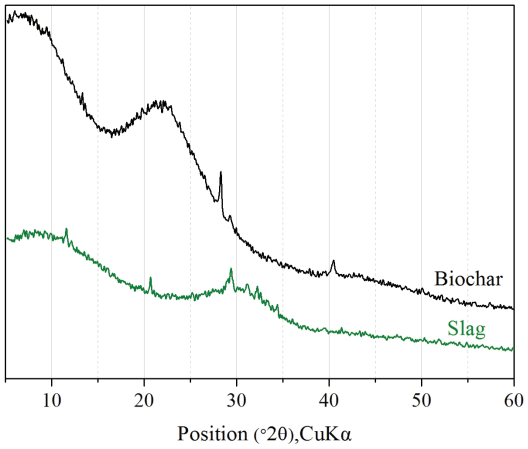

3 **XRD patterns of biochar and slag**

for slag and a porous microstructure for biochar. The XRD patterns of slag and biochar are illustrated in Figure 3, where both materials exhibit minor impurity peaks, with broad amorphous humps located at 25–35° for slag and 18–25° for biochar [6].

In this study, sodium hydroxide and sodium silicate were used as alkali activators for the AAS system at a mass ratio of 0.2. The sodium hydroxide had a purity above 98.0%, while the commercially supplied sodium silicate solution (Na_2O 9.5%, SiO_2 29%, water 61.5%) was chemically pure. Both activators were purchased from Daejung Chemicals & Metals Co., Ltd.

2.2 Methods

2.2.1 Preparation of alkali-activated paste and mortar specimens

Two types of specimens, paste and mortar, were prepared for different tests, and their mix proportions are listed in Table 2. The control paste and mortar were denoted as SB0 and SBM0, while biochar replaced slag at 1, 2, and 5 wt% in SB1, SB2, SB5 pastes and SBM1, SBM2, SBM5 mortars, respectively. All mixtures had identical liquid/binder, water/binder, and sand/binder ratios of 0.55, 0.46, and 2, respectively, with deionized water used to avoid ionic interference, and standard sand complying with ISO 679:2009 supplied by Société Nouvelle du Littoral.

According to the mix proportions in Table 2, sodium hydroxide, sodium silicate, and deionized water were first mixed, and after cooling to room temperature, slag and sand were added to prepare the control AAS paste and mortar. For biochar-containing mixtures, biochar was predispersed in the alkali solution using ultrasonic treatment before adding slag and sand, during which increasing bubble formation was observed with higher biochar content, as discussed in Section 3.6. All mixtures were mixed in a Hobart mixer at low speed for 2 min followed by high speed for 3 min, after which fresh specimens were tested or cast into molds, demolded after 24 h, and sealed for curing until the designated test age [7,8]. The specimen sizes, curing ages, and corresponding experimental items are listed in Table 3.

Table 2 **Mixing ratio design (mass%)**

Sample	Slag	Biochar	NaOH	Na_2SiO_3	Water	Sand	Liquid/ Binder	Water/ Binder	Sand/ Binder
SB0	100	–	3.2	16	35.8	–	0.55	0.46	–
SB1	99	1	3.2	16	35.8	–	0.55	0.46	–
SB2	98	2	3.2	16	35.8	–	0.55	0.46	–
SB5	95	5	3.2	16	35.8	–	0.55	0.46	–
SBM0	100	–	3.2	16	35.8	200	0.55	0.46	2
SBM1	99	1	3.2	16	35.8	200	0.55	0.46	2
SBM2	98	2	3.2	16	35.8	200	0.55	0.46	2
SBM5	95	5	3.2	16	35.8	200	0.55	0.46	2

Note: SB: Paste specimens; SBM: Mortar specimens.

Table 3 **Experimental items, specimen sizes, and curing ages**

	Experimental items	Specimen size (mm)	Test ages (days)
Reaction heat analyses (paste)	Isothermal calorimetry	–	0–7
Product analyses (paste)	XRD	–	28
	FTIR	–	28
	TG	–	28
	SEM	–	28
Workability (mortar/paste)	Flow test	–	Fresh
Mesoscopic image (mortar)	Microscope	50 × 50 × 50	28
Mechanical properties analyses (mortar)	Compressive strength	50 × 50 × 50	3, 7, 28
	UPV	40 × 40 × 160	3, 7, 28
Durability analyses (mortar)	Electrical resistivity	D100 × H200	3, 7, 28
	Chloride diffusion	D100 × H50	28

2.2.2 Isothermal calorimetry test

Following ASTM C1679 [9], the reaction heat of the paste was measured using a TAM-Air isothermal calorimeter, with heat flow and cumulative heat recorded for 7 d after transferring the freshly mixed paste into an ampoule, while both ambient and internal temperatures were maintained at 20°C.

2.2.3 Microscopic tests

The reaction products of the alkali-activated paste at 28 d were characterized by XRD (X-ray diffraction), FTIR (Fourier transform infrared spectroscopy), SEM (scanning electron microscopy), and TG (Thermogravimetry). For XRD and FTIR, paste samples were wet-milled with isopropanol, rinsed with acetone, and vacuum-dried to stop hydration, and crystalline phases and functional groups were analyzed using an X'pert-pro MPD diffractometer (5–80° 2θ) and a PerkinElmer FT-IR spectrophotometer (400–4000 cm^{-1}). The microstructure of the reaction products was examined by SEM using a Hitachi S-4800 microscope after surface pretreatment of vacuum-dried flakes. TG analysis was conducted using an SDT Q600 instrument over a temperature range of 20–1050°C at a heating rate of 10°C/min, with samples prepared using the same hydration-stopping procedure [10].

2.2.4 Properties tests

The engineering-scale properties of alkali-activated mortar were characterized by mesoscopic imaging, workability, mechanical performance, and durability. Mesoscopic surface images of 28-d hardened mortar were obtained using a LEICA Z16 APO optical microscope at 15× magnification, while the workability of fresh paste and mortar was evaluated by flow tests according to ASTM C1437 [11]. Compressive strength and ultrasonic pulse velocity (UPV) were measured following ASTM C109 [12] and ASTM C597 [13] using an SGB-F-200D compression tester and a Pundit Lab ultrasonic device (54 Hz), respectively. Durability was assessed by surface electrical resistivity and chloride migration resistance, with resistivity measured using a Wenner 50-mm Proceq Resipod and rapid chloride ion permeation tests conducted in accordance with ASTM C1202 [14] under 60 V for 24 h, using 0.3 mol/L NaOH and 3% NaCl solutions as anolyte and catholyte, respectively, and chloride penetration depth determined by $AgNO_3$ (0.1 N) color development.

3 Results

3.1 Reaction heat and reaction kinetics analysis

3.1.1 Reaction heat

Figure 4a,b presents the reaction heat flow and cumulative heat of SB0, SB1, SB2, and SB5 normalized by slag plus biochar mass, showing typical alkali-activation stages of initial dissolution, dormancy, acceleration, deceleration, and steady state, as illustrated in Figure 4a [15].

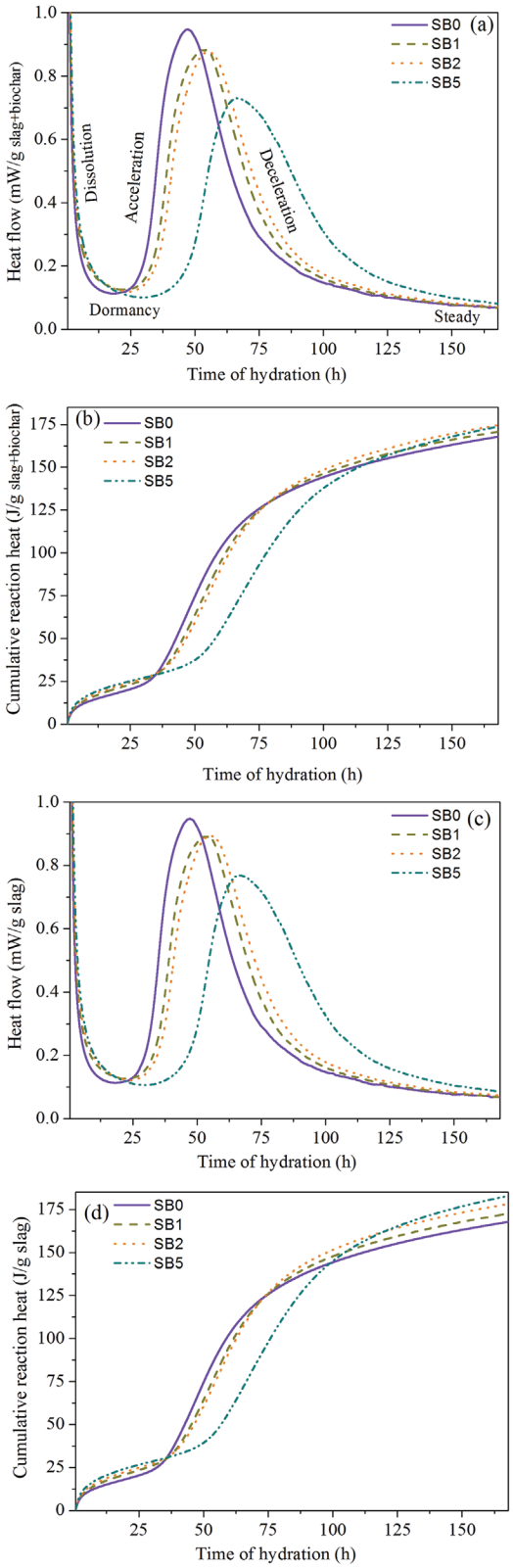

4 SB0, SB1, SB2, and SB5 normalized according to slag and biochar for (a) reaction heat flow and (b) cumulative reaction heat curve and normalized according to slag for (c) reaction heat flow and (d) cumulative reaction heat curve

Biochar addition prolonged the dormancy period and delayed the acceleration stage, with the effect most pronounced in SB5, while slag dilution and

alkali absorption by biochar pores reduced and delayed the main heat flow peak and caused peak broadening, especially at higher biochar contents. Despite these changes, Figure 4b shows similar cumulative reaction heats for SB0, SB1, SB2, and SB5, reaching 167.89, 170.86, 174.73, and 173.82 J/g slag + biochar, respectively.

Figure 4c,d shows the slag-normalized reaction heat flow and cumulative heat of SB0, SB1, SB2, and SB5, with heat flow trends consistent with those normalized by slag plus biochar (Figure 4c). Figure 4d reveals a crossover behavior, where cumulative heat decreased with increasing biochar content before ~100 h but became higher than the control thereafter, and the 7-d cumulative heat increased from 167.89 J/g slag for SB0 to 172.59, 178.30, and 182.98 J/g slag for SB1, SB2, and SB5, respectively, indicating that 2% and 5% biochar significantly promoted the 7-d alkali-activated reaction of slag.

3.1.2 Reaction kinetic analysis

As a stable carbon-based material, biochar does not participate in the alkali activation of slag, as confirmed in Sections 3.2, 3.3 and 3.5, but its porous structure significantly affects AAS reaction kinetics at different stages.

The alkali activation of slag by combined sodium hydroxide and sodium silicate involves rapid initial dissolution, where Ca–O bonds break more easily than Si–O and Al–O bonds under OH^- polarization, leading to preferential Ca^{2+} release and rapid reaction with SiO_4^{4-} ions.

During the dormancy stage, dissolution controls reaction kinetics, and in the AAS biochar system, partial absorption of alkali solution by biochar delays ion accumulation, prolonging the dormancy period compared with the control [16].

In the acceleration stage, extensive bond breakage and product formation occur, but in biochar-containing systems, absorption of OH^- and SiO_4^{4-} ions by biochar pores slows slag dissolution and reduces the reaction rate (Figure 5).

In the deceleration stage, although reaction products continue to form, the reaction becomes controlled by diffusion and kinetics, and the gradual release of OH^- and SiO_4^{4-} ions from biochar pores significantly extends this stage (Figure 5).

In the steady-state stage, product densification makes the reaction diffusion-controlled and extremely slow, and this stage is delayed in the AAS biochar system due to the effects of earlier stages.

Overall, early alkali absorption by biochar slows initial slag reaction, while later ion release sustains slag activation, whereas rapid early ion consumption in biochar-free systems leads to premature reaction slowdown, making biochar beneficial for enhancing the final degree of slag reaction.

3.2 XRD analyses

XRD analysis was conducted to examine the influence of biochar on the crystalline phases of alkali-activated products, and Figure 6 shows the XRD patterns of AAS biochar paste with different biochar contents at 28 d. As shown in Figure 6, all samples exhibited a broad hump near 29°, corresponding to semi-crystalline CASH (Calcium–Alumino–Silicate–Hydrate), the main AAS product formed from silicate ions in the alkali solution and Ca, Si, and Al from slag [17,18], with no obvious change in peak intensity among the mixtures. A weak and obscure peak near 31° was attributed to trace gehlenite magnesian phases [19]. No additional crystalline peaks were detected regardless of biochar content, indicating that biochar mainly plays a physical role by initially absorbing and later releasing alkali activators, affecting reaction kinetics but not altering the type of crystalline products, likely due to its chemical and physical stability and lack of participation in the alkali-activated reaction.

3.3 FTIR analyses

FTIR analysis was performed to further examine the influence of biochar on AAS products, and

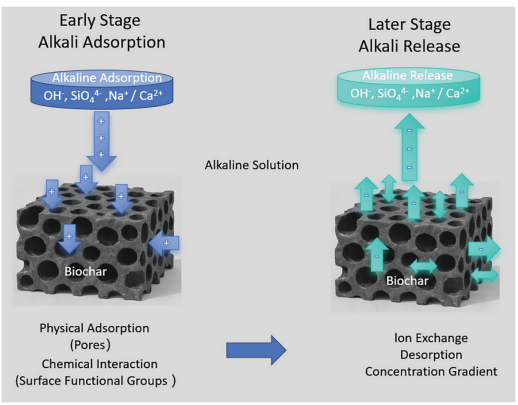

5 The "early absorption" and "later release" as the key mechanism of biochar

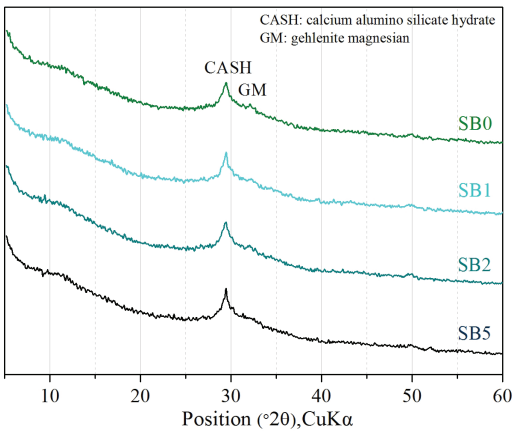

6 XRD patterns of AAS biochar-blended paste with different biochar substitution levels

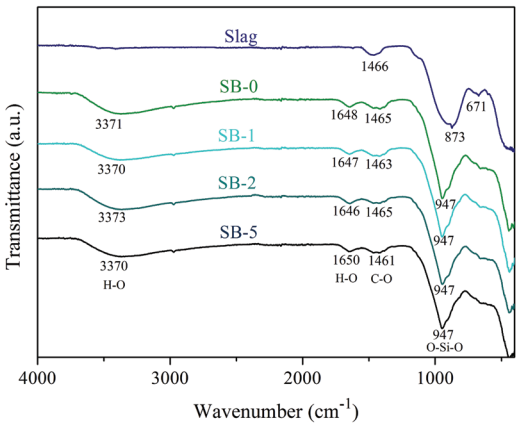

7 FTIR spectra of AAS biochar-blended paste at different biochar substitution levels at 28 d of age

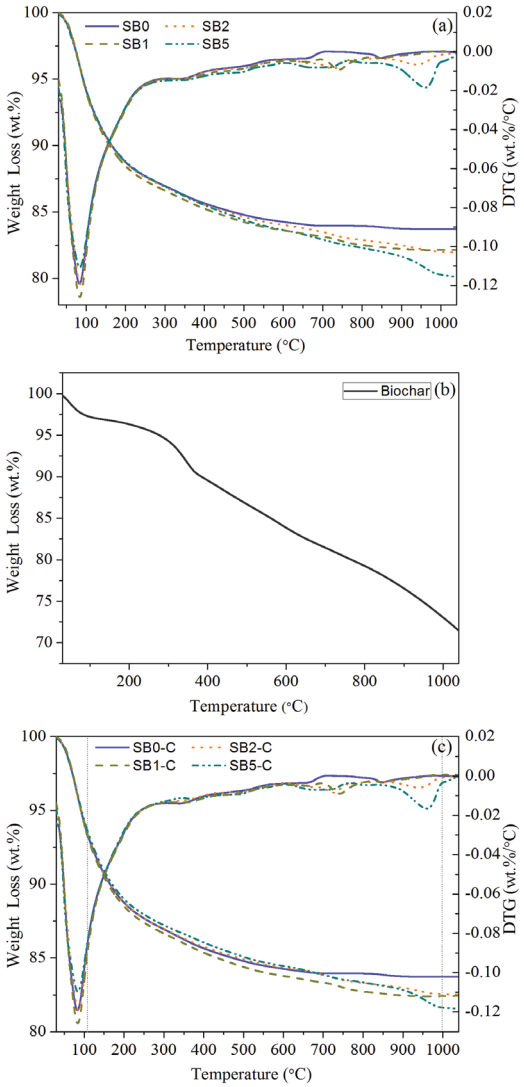

Figure 8 (a) TG and DTG curves, (b) TG curves of biochar, (c) corrected TG and DTG curves of the AAS biochar-blended paste with different biochar substitution levels for 28 d of curing

the spectra of pastes with different biochar contents are shown in Figure 7. All samples exhibited absorption bands near 3370 and 1650 cm^{-1} corresponding to bound water, a peak around 1461 cm^{-1} related to O–C–O stretching from carbonates in the slag, and a peak near 947 cm^{-1} associated with asymmetric O–Si–O stretching in CASH [20,21].

As shown in Figure 7, the positions and intensities of the main absorption peaks did not change significantly with biochar substitution, indicating that the functional group composition of AAS products remained unchanged, which is consistent with the XRD results in Figure 6. Since XRD and FTIR are qualitative techniques and unsuitable for quantitative analysis, TG tests were therefore conducted in the subsequent section to quantify the reaction products.

3.4 TG analyses

Figure 8a shows the TG and DTG (Derivative Thermogravimetry) curves of AAS biochar-blended paste with different biochar contents at 28 d, while Figure 8b presents the TG curve of biochar. Since biochar does not participate in alkali activation, chemically bound water originates solely from slag reaction and can be used to evaluate slag reaction degree; therefore, the mass loss of biochar must be excluded when calculating bound water per gram of reacted slag. Figure 8c illustrates the corrected TG and DTG curves after eliminating biochar weight loss, following the method described in Ref. [22], and the chemically bound water content was calculated using the following equation:

$$W_{water} = (W_{105} - W_{1000})/W_{1000} \times 100\% \qquad (1)$$

where W_{water} is the amount of bound water (g/g), W_{105} is the residual mass percentage at 105°C (%), and W_{1000} is the residual mass percentage at 1000°C (%).

As shown in Figure 8c, mass loss below 105°C is attributed to free water, while mass loss between 105 and 1000°C corresponds to CASH decomposition from alkali activation; therefore, the mass loss percentage and chemically bound water in this range were calculated and summarized in Table 4. The mass losses at 1000°C for SB0, SB1, SB2, and SB5 were 11.89, 13.53, 13.65, and 15.03 g/g, respectively, indicating that both mass loss and chemically bound water increased with biochar substitution, suggesting that biochar promoted late-stage CASH formation, consistent with the heat of reaction results.

3.5 SEM image analyses

Figure 9a–d presents SEM images of SB0, SB1, SB2, and SB5, respectively, while Figure 9f shows Energy-Dispersive X-ray Spectroscopy (EDX) results for representative areas of SB0 and SB5.

Table 4 Mass loss percentages obtained according to the corrected TG test result

Temperature (°C)	SB0	SB1	SB2	SB5
105	93.68	93.57	93.82	93.91
1000	83.72	82.41	82.55	81.63
105–1000	9.96	11.15	11.27	12.27
(105–1000)/1000	11.89	13.53	13.65	15.03

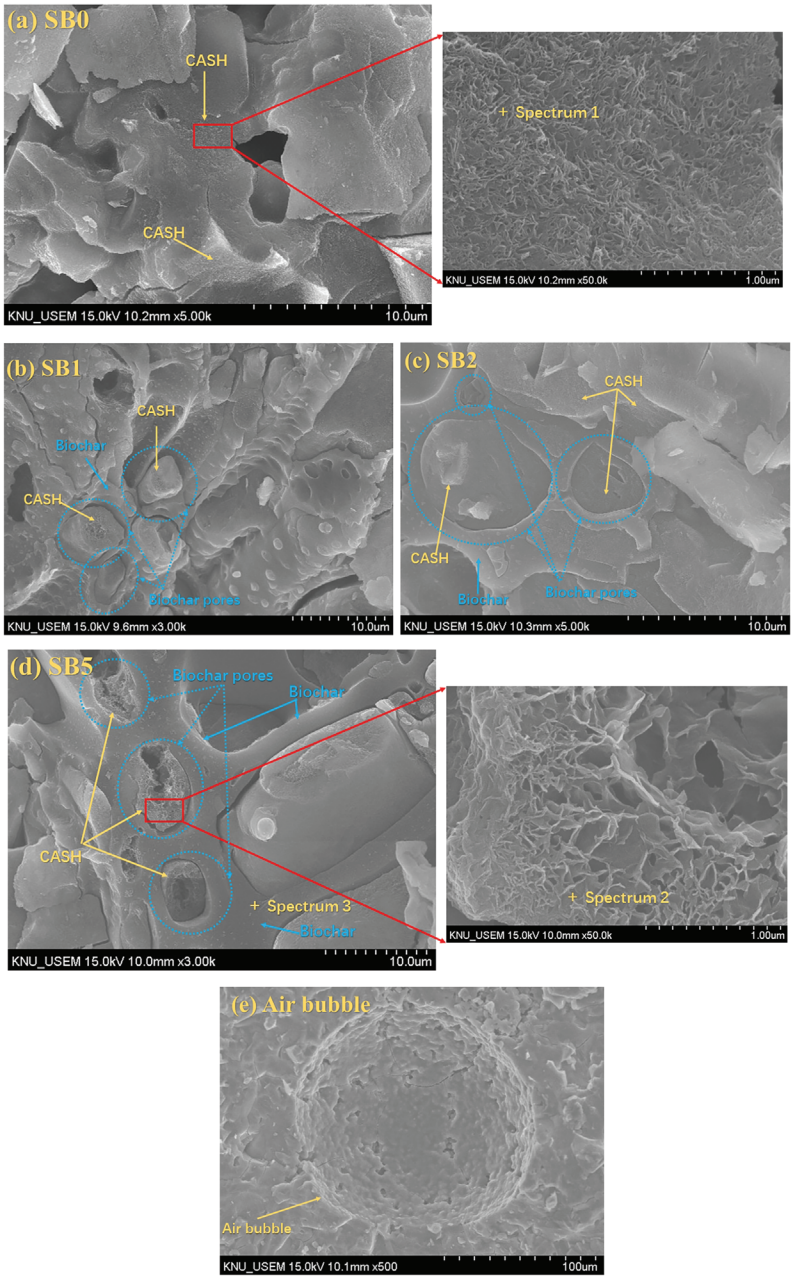

(f)

Spectrum 1 (for SB0)		
Element	Weight%	Atomic%
O	49.23	65.39
Na	4.63	4.28
Mg	1.55	1.36
Al	4.98	3.92
Si	17.18	13.00
S	1.18	0.78
Ca	21.26	11.27
Totals	100.00	

Spectrum 2 (for SB5)		
Element	Weight%	Atomic%
O	47.52	64.58
Na	4.62	4.37
Al	8.46	6.82
Si	11.18	8.65
S	1.80	1.22
K	2.68	1.49
Ca	23.74	12.88
Totals	100.00	

Spectrum 3 (for SB5)		
Element	Weight%	Atomic%
C	88.18	91.10
O	11.16	8.66
Al	0.14	0.06
Si	0.16	0.07
Ca	0.37	0.11
Totals	100.00	

9 SEM images of (a) SB0, (b) SB1, (c) SB2, (d) SB5, (e) and bubble in SB1. (f) EDX analysis results of the representative positions of SB0 and SB5 (spectrum 1 for SB0; spectrum 2 and spectrum 3 for SB5)

Compared with the smooth slag surface, SB0 exhibited a rough, corroded morphology after alkali activation, with honeycomb-like CASH observed at higher magnification, and EDX confirmed the presence of sodium-containing CASH.

As shown in Figure 9b–d, intact porous biochar was clearly observed in all AAS biochar systems, consistent with the XRD and FTIR results, confirming that biochar did not participate in the chemical reaction. SEM morphology and EDX analysis (Figure 9f) further revealed CASH formed within biochar pores, indicating that biochar pores provide space for alkali-activated reactions, in agreement with previous studies [23].

In addition, air bubbles were clearly observed in SB1, as shown in Figure 9e, confirming bubble formation during mixing of biochar with alkali solution (Section 2.2.1), which is consistent with the subsequent flowability results (Section 3.7) and mesoscopic image analysis of mortar specimens (Section 3.6).

3.6 Mesoscopic image of mortar specimens by microscopy

Figure 10 shows mesoscopic surface images of AAS and AAS biochar-blended mortars at 28 d, where SBM0 appears green and the surface color progressively darkens with increasing biochar content. Compared with SBM0, SBM1 exhibits visible air bubbles, whose number increases with higher biochar substitution, indicating that biochar introduces additional air into the AAS system, consistent with previous studies [23,24]. This behavior is attributed to the lower-density biochar initially floating in the alkali solution and gradually sinking during stirring and ultrasonic dispersion as its pores absorb the solution, expelling trapped gas and forming bubbles.

3.7 Workability

Figure 11 shows the flowability of AAS biochar paste and mortar at different biochar substitution levels, indicating similar trends for both systems, with the flow diameter initially increasing slightly and then decreasing as biochar content increases.

The slightly increased flowability at 1% biochar is attributed to entrained fine air bubbles, whereas the reduced flowability at 2% biochar results from partial absorption of the liquid alkali activator by biochar pores, and the pronounced decrease at 5% biochar is caused by excessive activator absorption due to the high biochar content.

3.8 Compressive strength and UPV

Figure 12a presents the compressive strength of AAS biochar mortars with varying biochar contents at different ages, while Figure 12b summarizes the relative compressive strengths normalized to the 3-d strength to facilitate comparison of

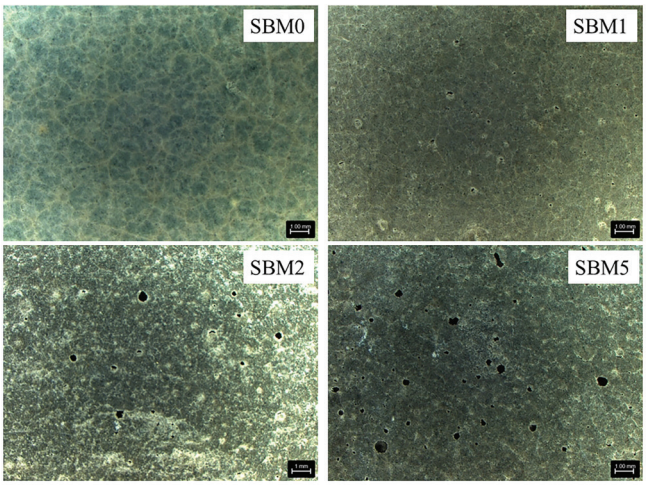

10 Mesoscopic images of AAS biochar mortar specimens at different substitution levels magnified 15 times

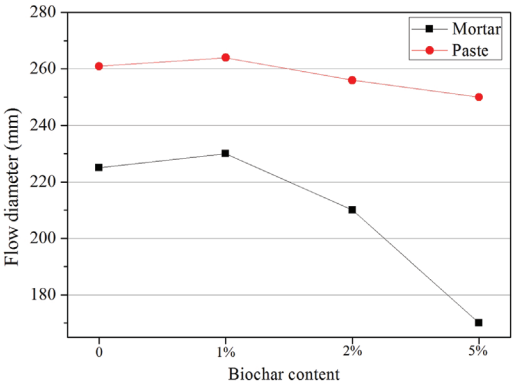

11 Flowability of AAS biochar paste and mortar with different biochar substitution levels

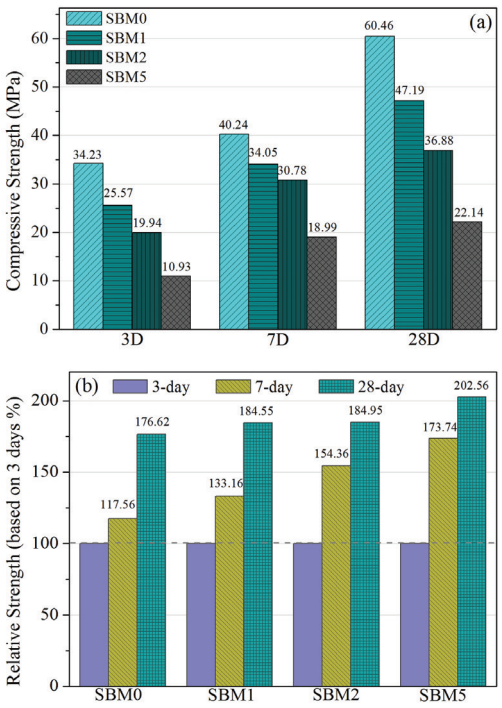

12 (a) Compressive strength and (b) relative compressive strength based on the specimen itself for 3 d

strength development with age, with the relative strength calculated as follows:

$$S_{relative} = S_{iD}/S_{3D} \times 100\% \quad (2)$$

where $S_{relative}$ is the relative compressive strength at the corresponding age, S_{iD} is the value of compressive strength at the corresponding ages of 3, 7, or 28 d, and S_{3D} is the value of compressive strength at 3 d.

As shown in Figure 12a, the compressive strength of AAS biochar mortars decreases with increasing biochar content at all ages, mainly due to bubble introduction associated with biochar addition.

As shown in Figure 12b, the relative compressive strength at 7 d increases with biochar substitution, indicating that the gradual release of alkali solution from biochar promotes early strength development, consistent with the 7-d heat evolution results. At 28 d, the relative strength further increases with biochar content, suggesting continued slow alkali release between 7 and 28 d, in agreement with the 28-d TG results. However, although curing age increases threefold from 7 to 28 d, the relative strength increase is much smaller, reflecting the rapid early slag reaction followed by a slowed steady-state reaction, as indicated by the heat of reaction in Figure 4.

Figure 13a presents the UPV results of AAS biochar mortars with different biochar contents at 3, 7, and 28 d, showing that UPV decreases with increasing biochar substitution, consistent with the compressive strength trend. This behavior reflects competing effects, including early-stage alkali absorption by biochar reducing slag reactivity at 3 d (Figure 4), later-stage alkali release enhancing slag reaction at 7 and 28 d (Figure 4), and air bubble introduction during mixing reducing UPV, with the negative effects dominating overall.

The relative UPV of each specimen with respect to the control at the same age was calculated using Equation (3), and the results are summarized in Figure 13b.

$$U_{relative} = U_{iD}/U_{SBM0\text{-}i} * 100\% \quad (3)$$

where $U_{relative}$ is the relative UPV at the corresponding age (i = 3, 7, 28 d). U_{iD} is the value of UPV of specimens SBM1, SBM2, and SBM5 at the corresponding age (i = 3, 7, and 28 d), and $U_{SBM0\text{-}i}$ is the value of UPV of specimen SBM0 at the corresponding age (i = 3, 7, and 28 d).

As shown in Figure 13b, the relative UPV of SBM1 increased from 94.8% at 3 d to 96.92% at 7 d and 97.9% at 28 d, while SBM2 and SBM5 increased from 93.48% and 79.62% at 3 d to 95.01% and 84.11% at 7 d and further to 95.22% and 88.75% at 28 d, respectively. With increasing curing age, the relative UPV of AAS biochar mortars increased because the gradual release of alkali solution from biochar pores continuously promoted product formation, thereby reducing the UPV gap between biochar-modified and control mortars, which is consistent with the relative compressive strength trend.

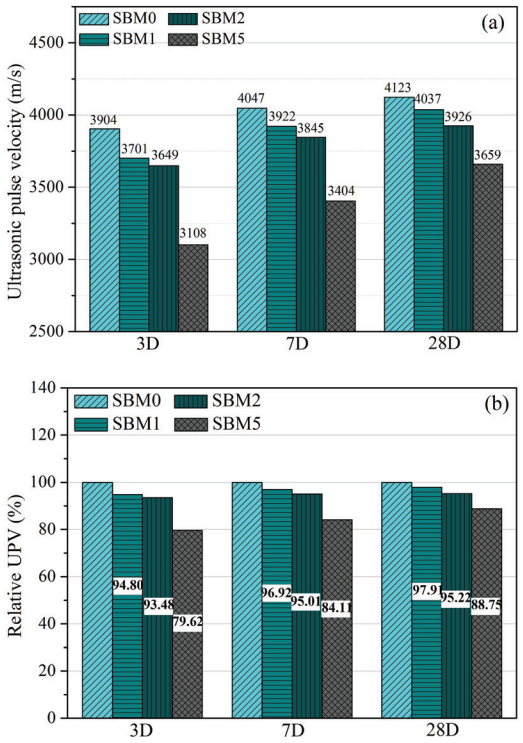

13 (a) UPV and (b) relative UPV based on the control specimens

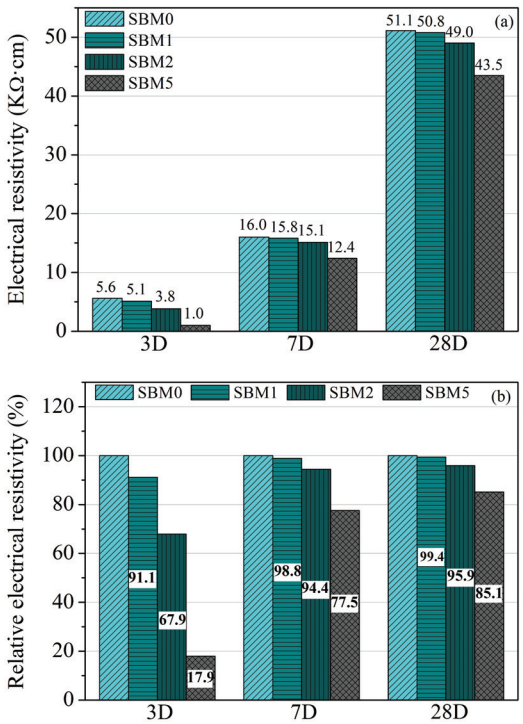

14 (a) Electrical resistivity and (b) relative electrical resistivity based on the control specimens

3.9 Electrical resistivity

Figure 14a shows the electrical resistivity of all alkali-activated mortars at different ages, where resistivity increases with curing age due to alkali consumption and formation of reaction products, while AAS biochar mortars exhibit lower resistivity with increasing biochar content at all ages because alkali solution retained in biochar pores increases the concentration of conductive ions.

The relative electrical resistivity of each specimen at the same age with respect to the control was calculated using Equation (4), and the results are summarized in Figure 14b.

$$E_{relative} = E_{iD}/E_{SBM0\text{-}i} * 100\% \quad (4)$$

where $E_{relative}$ is the relative electrical resistivity at the corresponding age (i = 3, 7, and 28 d). E_{iD} is the electrical resistivity of specimens SBM1, SBM2, and SBM5 at the corresponding age (i = 3, 7, and 28 d), and $E_{SBM0\text{-}i}$ is the electrical resistivity of specimen SBM0 at the corresponding age (i = 3, 7, and 28 d).

As shown in Figure 14b, the relative electrical resistivity of SBM1, SBM2, and SBM5 increased with age from 91.1%, 67.9%, and 17.9% at 3 d to 98.8%, 94.4%, and 77.5% at 7 d and further to 99.4%, 95.9%, and 85.1% at 28 d, indicating that the negative effect of biochar on resistivity diminished over time due to gradual alkali release sustaining the reaction. At 7 and 28 d, SBM1 and SBM2 exhibited electrical resistivity and relative resistivity comparable to SBM0, suggesting that low biochar contents (1% and 2%) had little influence on late-stage resistivity, whereas SBM5 consistently showed much lower relative resistivity than SBM0, indicating a detrimental effect of high biochar dosage.

3.10 Chloride diffusion

Figure 15 presents the chloride penetration depth (X_d) and the non-steady-state migration coefficient (D_{nssm}) of all mortar specimens calculated according to Ref. [25], showing X_d values of 4.48, 5.63, 6.54, and 13.79 mm and corresponding D_{nssm} values of 0.93, 1.19, 1.40, and 3.12 × 10−12 m²/s for SBM0, SBM1, SBM2, and SBM5, respectively. With increasing biochar content, D_{nssm} increased slightly for SBM1 and SBM2 but rose markedly for SBM5, indicating that the additional bubbles introduced by biochar, as discussed in Section 3.6, accelerated chloride diffusion.

According to the D_{nssm}-based chloride resistance classification [26], only SBM5 falls into the "very high" chloride resistance category, as shown in Figure 15, whereas SBM1 and SBM2, despite slightly higher D_{nssm} values than SBM0, are still classified as "extremely high," indicating excellent durability. This suggests that small amounts of biochar have a limited impact on chloride diffusion, consistent with the electrical resistivity results.

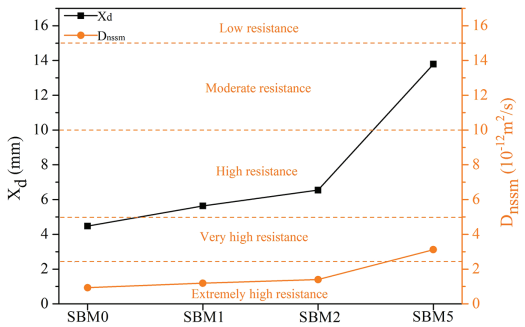

15 Chloride penetration depth and chloride non-steady-state migration coefficient of AAS biochar mortar with different biochar substitution levels

4 Discussion

4.1 Relationships between the results of multi-method studies

Figure 16a shows exponential fitting between compressive strength and UPV at all ages, while Figure 16b shows linear fitting between electrical resistivity and D_{nssm}, indicating a positive correlation between UPV and strength and a negative correlation between resistivity and D_{nssm}, with R^2 values of 0.9196 and 0.98, respectively. XRD, FTIR, and SEM results confirmed that biochar did not participate in the alkali-activated reaction, whereas reaction heat

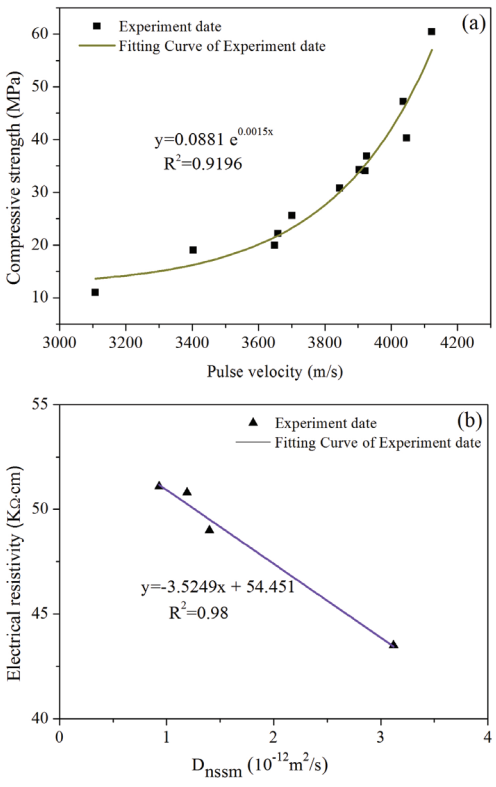

16 (a) Fitting curves for the results of compressive strength and UPV at all curing ages and (b) fitting curves for the results of 28-d electrical resistivity and D_{nssm}

and TG results demonstrated that biochar promoted slag activation, and workability, mesoscopic images, and SEM observations revealed bubble incorporation, with the consistent trends across multiple techniques confirming the scientific reliability of the characterization of AAS biochar composites.

4.2 Additional considerations on the application of biochar to alkali-activated systems

As industrial and agricultural by-products, slag and biochar show strong potential for sustainable construction. This study demonstrates that biochar remains stable under alkali-activated conditions and affects AAS reaction kinetics by early alkali absorption and later release, delaying early reactions but promoting late-age slag activation. Engineering tests indicate that changes in mechanical properties and durability are mainly linked to air bubble formation and reduced early-age activation, while moderate biochar additions (1–2 wt%) showed acceptable durability and partial recovery of later-age strength, confirming the feasibility of partial slag replacement. Air bubble formation during biochar dispersion was identified as a key factor influencing performance, and practical mitigation measures include defoamers and biochar pre-soaking, with the latter also retaining internal curing benefits. Overall, biochar contents of 1–2 wt% are most practical, as SBM1 and SBM2 maintained good durability, whereas 5 wt% caused bubble-induced deterioration.

4.3 The limitations of the research

First, this study examined only one biochar with a specific source, production process, and particle size, and since biochar properties strongly depend on feedstock and pyrolysis conditions, the results may not be directly applicable to other biochar.

Second, the alkali-activated slag system employed a single activator composition and fixed mix proportions, and the effects of different activator chemistries, alkalinity levels, or mixture designs on biochar–AAS interactions were not considered.

Third, durability assessment mainly focused on electrical resistivity and chloride migration, while other important durability aspects of alkali-activated materials, such as carbonation resistance, freeze–thaw behavior, sulfate attack, and long-term dimensional stability, were not investigated.

Fourth, although alkali-activated slag systems are known to exhibit significant shrinkage, the shrinkage behavior of biochar-modified AAS was not investigated in this study. Given the porous structure of biochar and its potential internal curing and moisture-retention effects, biochar is expected to have the capacity to mitigate both autogenous and drying shrinkage. Future work will therefore systematically examine shrinkage behavior under varying biochar contents and curing conditions.

5 Conclusions

This study investigated the effects of biochar on the reaction kinetics, microstructure, and performance of alkali-activated slag (AAS). The main conclusions are as follows:

1. Biochar modified the reaction kinetics of AAS by initially absorbing the alkali solution and releasing it at later ages, leading to a broadened heat-flow peak and increased cumulative reaction heat, which promoted the sustained activation of slag.
2. XRD and FTIR results confirmed that the primary reaction product remained C-A-S-H regardless of biochar content, indicating that biochar played a physical role without altering the chemical nature of the alkali-activated products.
3. Corrected TG and SEM analyses showed increased bound water content and C-A-S-H formation at later ages, with biochar pores providing internal space that facilitated continued slag activation.
4. The incorporation of biochar introduced air bubbles, which influenced fresh and hardened properties, resulting in non-monotonic changes in flowability and a reduction in absolute compressive strength.
5. Despite the strength reduction, biochar-modified AAS exhibited improved relative strength, UPV development, and acceptable chloride resistance at later ages, demonstrating that controlled biochar incorporation can maintain durability while enhancing long-term reaction efficiency.

Acknowledgement

Not applicable.

Funding Statement

This research was supported by National Natural Science Foundation of China (Grant No. 42306229). This research was supported by the Korea Institute of Energy Technology Evaluation and Planning funded by the Ministry of Trade, Industry and Energy (No. 2025-02314098) of the Republic of Korea. This research was supported by the Regional Innovation System & Education (RISE) program through the Gangwon RISE Center, funded by the Ministry of Education (MOE) and the Gangwon State (G.S.), Republic of Korea (2025-RISE-10-002).

Author Contributions

Xu Yang: conceptualization, methodology, investigation, data curation, writing—review & editing. Feng Sun: conceptualization, methodology, investigation, data curation, writing—review & editing. Ki-Bong Park: investigation, validation, writing—review & editing. Xiao-Yong Wang: conceptualization, supervision, validation, resources, project

administration, funding acquisition, writing—review & editing. All authors reviewed and approved the final version of the manuscript.

Availability of Data and Materials

Data available on request from the authors.

Ethics Approval

Not applicable.

Conflicts of Interest

The authors declare no conflicts of interest.

REFERENCES

[1] Zuo Y, Chen Y, Liu C, Gan Y, Göbel L, Ye G, et al. Modeling and simulation of alkali-activated materials (AAMs): a critical review. Cem Concr Res. 2025;189:107769. doi:10.1016/j.cemconres.2024.107769.

[2] Sun Y, Liu Z, Ghorbani S, Ye G, De Schutter G. Fresh and hardened properties of alkali-activated slag concrete: the effect of fly ash as a supplementary precursor. J Clean Prod. 2022;370:133362. doi:10.1016/j.jclepro.2022.133362.

[3] Praneeth S, Guo R, Wang T, Dubey BK, Sarmah AK. Accelerated carbonation of biochar reinforced cement-fly ash composites: enhancing and sequestering CO_2 in building materials. Constr Build Mater. 2020;244:118363. doi:10.1016/j.conbuildmat.2020.118363.

[4] Cuthbertson D, Berardi U, Briens C, Berruti F. Biochar from residual biomass as a concrete filler for improved thermal and acoustic properties. Biomass Bioenergy. 2019;120:77–83. doi:10.1016/j.biombioe.2018.11.007.

[5] Akinyemi BA, Adesina A. Recent advancements in the use of biochar for cementitious applications: a review. J Build Eng. 2020;32:101705. doi:10.1016/j.jobe.2020.101705.

[6] Waqas M, Aburiazaiza AS, Miandad R, Rehan M, Barakat MA, Nizami AS. Development of biochar as fuel and catalyst in energy recovery technologies. J Clean Prod. 2018;188:477–88. doi:10.1016/j.jclepro.2018.04.017.

[7] Zhang H, Xu Y, Gan Y, Chang Z, Schlangen E, Šavija B. Combined experimental and numerical study of uniaxial compression failure of hardened cement paste at micrometre length scale. Cem Concr Res. 2019;126:105925. doi:10.1016/j.cemconres.2019.105925.

[8] Ge Z, Tawfek AM, Zhang H, Yang Y, Yuan H, Sun R, et al. Influence of an extrusion approach on the fiber orientation and mechanical properties of engineering cementitious composite. Constr Build Mater. 2021;306(1):124876. doi:10.1016/j.conbuildmat.2021.124876.

[9] ASTM C1679-22. Standard practice for measuring hydration kinetics of hydraulic cementitious mixtures using isothermal calorimetry. West Conshohocken, PA, USA: ASTM; 2023.

[10] Zhang J, Chen T, Gao X. Incorporation of self-ignited coal gangue in steam cured precast concrete. J Clean Prod. 2021;292:126004. doi:10.1016/j.jclepro.2021.126004.

[11] ASTM C1437-20. Standard test method for flow of hydraulic cement mortar. West Conshohocken, PA, USA: ASTM; 2020.

[12] ASTM C109/C109M-20. Standard test method for compressive strength of hydraulic cement mortars (using 2-in. or [50-mm] cube specimens). West Conshohocken, PA, USA: ASTM; 2020.

[13] ASTM C597-16. Standard test method for pulse velocity through concrete. West Conshohocken, PA, USA: ASTM; 2023.

[14] ASTM C1202-19. Standard test method for electrical indication of concrete's ability to resist chloride ion penetration. West Conshohocken, PA, USA: ASTM; 2022.

[15] Zheng Y, Zhong H, Sun K, Shen B, Cui K, Zhao Y, et al. Effect of composite activator on hydration kinetics and micromechanical properties of alkali-activated slag. Cem Concr Compos. 2025;160:106047. doi:10.1016/j.cemconcomp.2025.106047.

[16] Kong F, Xu R, Wang A, Hong T, Shi X. Effects of different activators on workability, mechanical properties and microstructure of alkali-activated slag-copper slag. Constr Build Mater. 2025;463:140151. doi:10.1016/j.conbuildmat.2025.140151.

[17] Li C, Sun H, Li L. A review: the comparison between alkali-activated slag (Si+Ca) and metakaolin (Si+Al) cements. Cem Concr Res. 2010;40(9):1341–9. doi:10.1016/j.cemconres.2010.03.020.

[18] Fu J, Bligh MW, Shikhov I, Jones AM, Holt C, Keyte LM, et al. A microstructural investigation of a Na_2SO_4 activated cement-slag blend. Cem Concr Res. 2021;150:106609. doi:10.1016/j.cemconres.2021.106609.

[19] Cao R, Zhang S, Banthia N, Zhang Y, Zhang Z. Interpreting the early-age reaction process of alkali-activated slag by using combined embedded ultrasonic measurement, thermal analysis, XRD, FTIR and SEM. Compos Part B Eng. 2020;186:107840. doi:10.1016/j.compositesb.2020.107840.

[20] Palacios M, Gismera S, Alonso MM, d'Espinose de Lacaillerie JB, Lothenbach B, Favier A, et al. Early reactivity of sodium silicate-activated slag pastes and its impact on rheological properties. Cem Concr Res. 2021;140:106302. doi:10.1016/j.cemconres.2020.106302.

[21] Alventosa KML, White CE. The effects of calcium hydroxide and activator chemistry on alkali-activated metakaolin pastes. Cem Concr Res. 2021;145:106453. doi:10.1016/j.cemconres.2021.106453.

[22] Yang X, Wang XY. Strength and durability improvements of biochar-blended mortar or paste using accelerated carbonation curing. J CO_2 Util. 2021;54:101766. doi:10.1016/j.jcou.2021.101766.

[23] Yang X, Wang XY. Hydration-strength-durability-workability of biochar-cement binary blends. J Build Eng. 2021;42:103064. doi:10.1016/j.jobe.2021.103064.

[24] Praneeth S, Saavedra L, Zeng M, Dubey BK, Sarmah AK. Biochar admixtured lightweight, porous and tougher cement mortars: mechanical, durability and micro computed tomography analysis. Sci Total Environ. 2021;750:142327. doi:10.1016/j.scitotenv.2020.142327.

[25] Pontes J, Real S, Alexandre Bogas J. The rapid chloride migration test as a method to determine the chloride penetration resistance of concrete in marine environment. Constr Build Mater. 2023;404:133281. doi:10.1016/j.conbuildmat.2023.133281.

[26] Afroughsabet V, Biolzi L, Monteiro PJM. The effect of steel and polypropylene fibers on the chloride diffusivity and drying shrinkage of high-strength concrete. Compos Part B Eng. 2018;139:84–96. doi:10.1016/j.compositesb.2017.11.047.